Photoacoustics 32 (2023) 100531

Contents lists available at ScienceDirect

Photoacoustics

journal homepage: www.elsevier.com/locate/pacs

Dynamic 2-deoxy-D-glucose-enhanced multispectral optoacoustic tomography for assessing metabolism and vascular hemodynamics of breast cancer

Zheng Han [a,b], William M. MacCuaig [a,c], Metin N. Gurcan [d], Juan Claros-Sorto [a], Tabitha Garwe [e], Christina Henson [f], Jennifer Holter-Chakrabarty [f], Bethany Hannafon [g], Vishal Chandra [g], Elizabeth Wellberg [h], Lacey R. McNally [a,*]

[a] Department of Surgery, University of Oklahoma Health Science Center, Oklahoma City, OK 73104, USA
[b] Center for Health Systems Innovation, Oklahoma State University, Stillwater, OK 74078, USA
[c] Department of Bioengineering, University of Oklahoma, Norman, OK 73019, USA
[d] Center for Biomedical Informatics, Wake Forest Baptist Health, Winston-Salem, NC 27101, USA
[e] Department of Biostatistics and Epidemiology, University of Oklahoma Health Science Center, Oklahoma City, OK 73104, USA
[f] Department of Internal Medicine, University of Oklahoma Health Science Center, Oklahoma City, OK 73104, USA
[g] Department of Obstetrics and Gynecology, University of Oklahoma Health Science Center, Oklahoma City, OK 73104, USA
[h] Department of Pathology, University of Oklahoma Health Science Center, Oklahoma City, OK 73104, USA

ARTICLE INFO

Keywords:
Multispectral optoacoustic tomography, optoacoustic imaging
Photoacoustic imaging
Breast cancer
2-deoxyglucose
Pharmacokinetics
Extended Tofts model
Reference region model
Metabolism
Hemodynamics

ABSTRACT

Clinical tools for measuring tumor vascular hemodynamics, such as dynamic contrast-enhanced MRI, are clinically important to assess tumor properties. Here we explored the use of multispectral optoacoustic tomography (MSOT), which has a high spatial and temporal resolution, to measure the intratumoral pharmacokinetics of a near-infrared-dye-labeled 2-Deoxyglucose, 2-DG-800, in orthotropic 2-LMP breast tumors in mice. As uptake of 2-DG-800 is dependent on both vascular properties, and glucose transporter activity – a widely-used surrogate for metabolism, we evaluate hemodynamics of 2-DG-MP by fitting the dynamic MSOT signal of 2-DG-800 into two-compartment models including the extended Tofts model (ETM) and reference region model (RRM). We showed that dynamic 2-DG-enhanced MSOT (DGE-MSOT) is powerful in acquiring hemodynamic rate constants, including K^{trans} and $K_{ep,}$ via systemically injecting a low dose of 2-DG-800 (0.5 μmol/kg b.w.). In our study, both ETM and RRM are efficient in deriving hemodynamic parameters in the tumor. Area-under-curve (AUC) values (which correlate to metabolism), and K^{trans} and K_{ep} values, can effectively distinguish tumor from muscle. Hemodynamic parameters also demonstrated correlations to hemoglobin, oxyhemoglobin, and blood oxygen level (SO_2) measurements by spectral unmixing of the MSOT data. Together, our study for the first time demonstrated the capability of DGE-MSOT in assessing vascular hemodynamics of tumors.

1. Introduction

Cancer cells are known to exploit elevated glucose metabolism to allow them to proliferate and avoid apoptosis. This high glucose metabolism is the underpinning of widely used [^{18}F]FDG-positron emission tomography (PET), among other imaging techniques [1,2], for tumor detection [3,4]. While tumors may develop abundant vasculature for nutrient and oxygen supply, their blood flow and metabolism may not increase in parallel. This asynchrony results in hypoxia that correlates with tumor aggressiveness and resistance to treatment [5,6]. Hence, tumor vascular hemodynamics and metabolism are two important characteristics of the tumor microenvironment linked to cancer progression [7,8].

Currently, vascular hemodynamics and metabolism are usually measured in two separate imaging scans, namely dynamic contrast-enhanced magnetic resonance imaging (DCE-MRI) for evaluating tumor vascular hemodynamics [9–11] and [^{18}F]FDG-PET for metabolism measurement. In DCE-MRI, pharmacokinetic modeling of the microcirculation of contrast agents, usually gadolinium-based agents, shed light on underlying tumor vasculature properties, such as

---

* Corresponding author.
E-mail address: lacey_mcnally@hotmail.com (L.R. McNally).

https://doi.org/10.1016/j.pacs.2023.100531
Received 13 February 2023; Received in revised form 22 June 2023; Accepted 8 July 2023

perfusion, permeability, and microvascular density properties of the tumor [12]. The hemodynamic parameters, e.g., rate constants including K^{trans} and K_{ep}, have been significant predictors of treatment response in a variety of malignancies [13,14]. Concerns on potential gadolinium toxicity and deposition [15–17] limit repeated use of gadolinium-based contrast agents, particularly for those with impaired renal function, hampering its capability to closely monitor tumor development during treatment.

A previous study explored modeling dynamic [^{18}F]FDG-PET signal to derive hemodynamic parameters, in addition to the metabolism measurement, as surrogates of tumor aggressiveness or prognosis factors [18]. Despite showing potential to derive hemodynamic parameters with strong correlations to those provided by DCE-MRI, the ionizing radiation and low temporal and spatial resolution of [^{18}F]FDG-PET compromise its clinical utility as a replacement for DCE-MRI. Studies have explored labeling 2-deoxyglucose (2-DG), another glucose analog, with fluorescent dyes to map metabolic profiles [19] using fluorescence imaging. However, the limited penetration depth of fluorescence imaging makes it difficult to accurately analyze tumor tissues embedded at more than 8 mm below the skin. Dynamic modeling of 2-DG within the tumor has been understudied due to the inability of fluorescence imaging to study 2-DG microcirculation within the tumor, muscle, and artery simultaneously, which is critical for accurate modeling of the pharmacokinetics.

Multispectral optoacoustic tomography (MSOT) is an emerging imaging modality capable of imaging clinically significant depth with a high spatial and temporal resolution [20–22]. For example, it has been shown that MSOT can image through > 5 cm of tissue [23,24], enabling tomographic imaging with optical contrast at depths usually restricted to optical imaging and ultrasound [23–27]. MSOT detects both endogenous and exogenous chromophores through heat production and thermoelastic expansion caused by near-infrared (NIR) light absorption. The use of optoacoustic effects overcomes the depth limitations of optical imaging while allowing detection of multiple agents and providing the high resolution of ultrasound imaging. MSOT can monitor levels of deoxy-hemoglobin, oxy-hemoglobin, collagen, fat, etc., in tissues, meanwhile allowing the detecting multiple contrast agents, nanoparticles, labeled antibodies/peptides, and small molecules [28–36]. Previously, our group has reported the use of MSOT for pharmacokinetics modeling of an exogenous dye, hypoxia-specific dye Hypoxisense HS680 [37], within the tumor using region-of-interest (ROI)-based analyses. However, ROI-based analysis is unable to provide intratumoral heterogeneity of the pharmacokinetic parameters, and how these parameters correlate to endogenous chromophores in a voxel-based manner remains unknown. Thus far, simultaneous evaluation of tumor vascular hemodynamics and glucose metabolism using MSOT has not been studied.

Herein, we aim to explore the use of 2-DG-800, a commercially available dye that has been previously employed as an exogenous MSOT agent for tumor detection [38], to simultaneously measure vascular hemodynamics and metabolism of breast cancer tumors using MSOT. We focused on establishing a voxel-based method for analyzing DGE-MSOT data and comparing two common two-compartmental models for deriving hemodynamic rate constants, namely the extended Tofts model (ETM) [39] and reference region model (RRM) [40]. We also evaluated correlations of hemodynamic rate constants in tumors to levels of endogenous chromophores.

2. Materials and methods

2.1. Cell culture and mouse breast tumor model

The human triple-negative breast cancer cell line, 2-LMP was maintained in DMEM medium (GIBCO, Gaithersburg, MD) supplemented with 10 % fetal bovine serum (FBS). Four female athymic mice (20 g of body weight and 4 weeks of age) were purchased from Charles River Laboratories (Wilmington, NC, USA). Mice were injected with 5×10^5 2-LMP cells in the upper mammary fat pad. Mice were housed under pathogen-free conditions following the guidelines of the American Association for Laboratory Animal Care. When tumors were 7–10 mm in diameter (~ 30 days post-injection), MSOT was performed in accordance with the standards of the University of Oklahoma Health Sciences Center (OUHSC), and the Institutional Animal Care and Use Committee of OUHSC.

2.2. Multispectral optoacoustic tomography (MSOT) imaging

Mice were scanned using MSOT inVision 512-TF (iThera Medical GmbH, Munich, Germany) equipped with a 512-element, toroidal, ring-shaped transducer array using 10 Hz laser pulses and wavelengths ranging from 680 to 900 nm. Mice were kept under anesthesia with 1.5 % isoflurane and a 30-gauge catheter was inserted into the lateral tail vein for injection. Mice were anesthetized for > 10 min to ensure stable physiology before MSOT acquisition. A single-slice axial image was repeatedly acquired at the center tumor position for 4 min, and 10 nmol of 2-DG-800 (LI-COR Biosciences, Lincoln, NE, Lincoln, NE) in 200 μL PBS (pH $= 7.4$) was then manually injected in bolus for 1 min. Mice were scanned at a temporal resolution of 15 s for 40 min. The timeline of imaging is shown in Fig. 1**A**.

2.3. Image reconstruction and spectral unmixing

MSOT images were reconstructed using the curve-driven-based model-matrix inversion (CDMMI) algorithm [41] using the MSOT-RAFT Matlab package [42]. Signals of deoxyhemoglobin (Hb), oxyhemoglobin (HbO_2) and 2-DG-800 in each pixel were separated using a linear spectral unmixing method by referencing the corresponding absorption spectra. SO_2, a parameter considered to describe blood oxygen level, was calculated using the equation $SO_2 = HbO_2/(HbO_2 + Hb)$[43].

2.4. Pharmacokinetic modeling

The two-compartmental extended Tofts model (ETM) [39] (Eq. (1)) and non-linear reference region model (RRM) [40] (Eq. (2)) were used to analyze the time-course signal of 2-DG-800. A custom-written MATLAB package adapted based on the fitdce function [44] previously used for analyzing DCE-MRI data, was used for curve-fitting. In brief, the Tofts model describes the kinetics of contrast agents within the tumor at a given time point, $C_{tumor}(t)$ with respect to the contrast agent in plasma, $C_{plasma}(t)$. The rate constant K^{trans} (min^{-1}) describes the rate at which the contrast agent in the plasma is taken up into the tumor space, and K_{ep} describes the rate at which the agent returns from the tumor space into the plasma. The time-dependent probe concentration in tumor using the extended Tofts model can be described as:

$$C_{tumor}(t) = v_{plasma} \bullet C_{plasma}(t) + K^{trans,tumor} \bullet \quad e^{-t \bullet K_{ep}} \qquad e^{-t \bullet K_{ep,tumor}} \\ * C_{plasma}(t) \tag{1}$$

where * denotes convolution, and v_{plasma} denotes plasma volume in the tumor.

In RRM, $C_{tumor}(t)$, with respect to the probe concentration in reference region $C_{RR}(t)$, can be described as:

$$C_{tumor}(t) = \frac{K^{trans,tumor}}{K^{trans,RR}} \bullet C_{RR}(t) + \frac{K^{trans,tumor}}{K^{trans,RR}} \\ \bullet \left(K_{ep,RR} - K_{ep,tumor}\right) \bullet e^{-t \bullet K_{ep,tumor}} * C_{RR}(t) \tag{2}$$

where $K^{trans,tumor}$, $K^{trans,RR}_{,}$ $K_{ep,tumor}$ and $K_{ep,RR}$ denote the K^{trans} and K_{ep} values of the tumor and reference region. The reference regions used were muscle tissues in the current study.

The relationship between MSOT signal S, detected at certain exci-

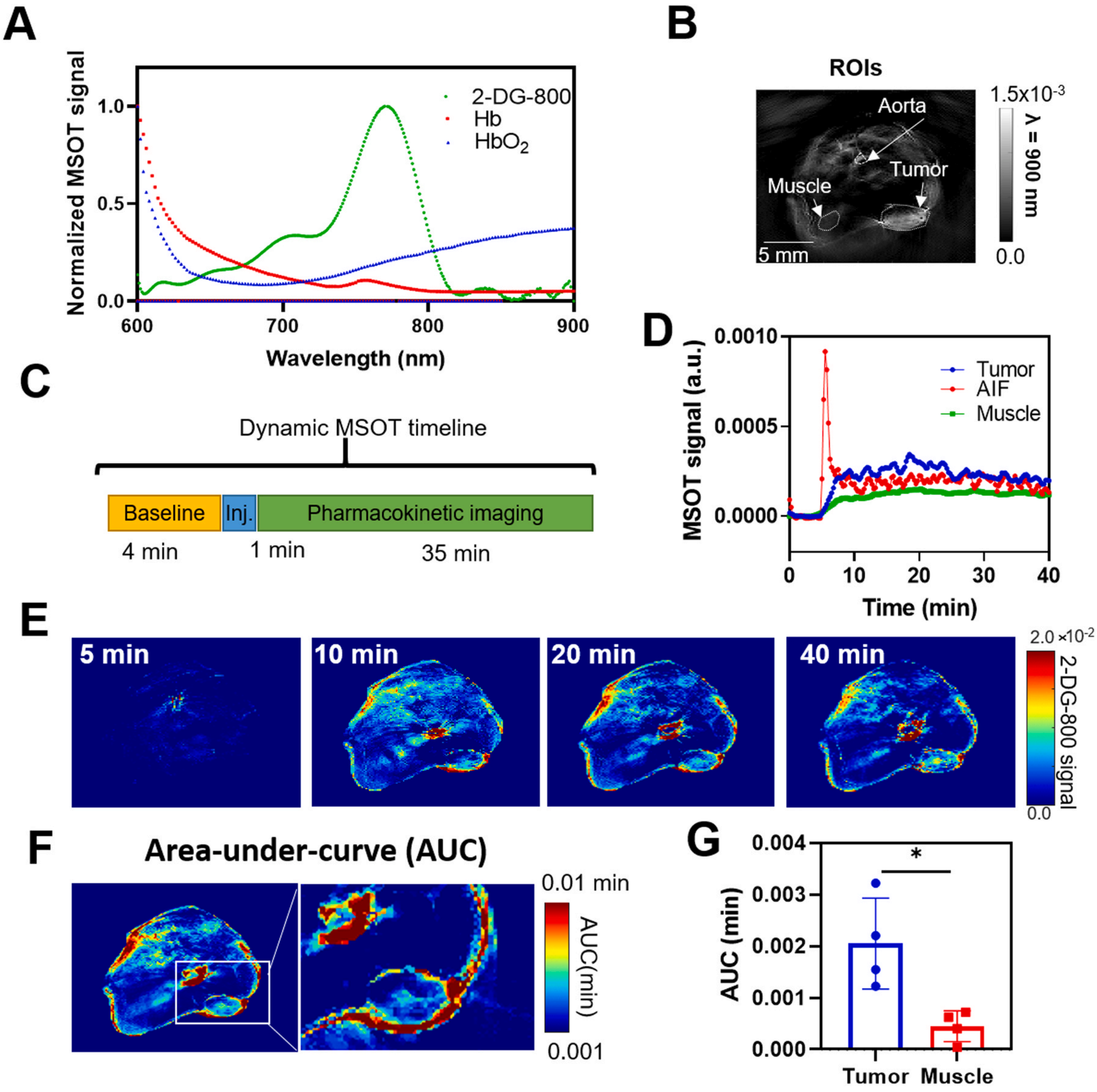

Fig. 1. Dynamic 2-DG enhanced MSOT (DGE-MSOT) readily detects breast tumors based on 2-DG accumulation. A. Normalized MSOT signal spectra of 2-DG-800, deoxyhemoglobin (Hb) and oxyhemoglobin (HbO_2). **B.** Selection of ROIs based on an axial MSOT image of the mouse at the wavelength (λ) of 900 nm. **C.** Timeline of dynamic 2-DG enhanced MSOT. **D.** Representative dynamic signal curves of tumor, muscle and aorta regions. **E.** Representative MSOT images of 2-DG-800 distribution at 5 (right after injection, see **c**),10, 20 and 40 min. **F.** Area-under-curve (AUC) maps on a representative mouse. **G.** Comparison of AUC values of tumor and muscle (n = 4, *: $P = 0.0392$, paired Student's t-test).

tation wavelength (λ), position (r) and time (t) can be expressed using Eq. (3) [45],

$$S(\lambda, r, t) = \Gamma \bullet \Phi(\lambda, r) \bullet \mu(\lambda, r) \bullet \varepsilon(\lambda) \bullet C_{\mathrm{IR800CW-2-DG-800}}(t) \tag{3}$$

where Γ is the Gruneisen parameter; Φ(λ,r) is the light fluence (J/cm^2), μ(λ,r) is the absorption coefficient (cm^{-1}), ε(λ) is the molar extinction coefficient ($L\ mol^{-1}\ cm^{-1}$), and $C_{2\text{-DG-800}}$ is the concentration ($mol\ L^{-1}$) of 2-DG-800. Hence, the MSOT signal is linear to the concentration of 2-DG-800 in tissues, and $C_{2\text{-DG-800}}(t)$ can be simply replaced by MSOT signal intensity, S(t). By referencing MSOT images at 900 nm (Fig. 1**B**), at which HbO_2 signal is dominant, regions of interest were drawn around tumor, anterior spinal artery, and muscle. The dynamic 2-DG-800 signal in the spinal aorta was referred to as the arterial input function (AIF, denoted as C_{plasma} in Eq. (1)) which, together with $C_{tumor}(t)$ or $C_{muslce}(t)$, were used to solve the equation (Eq. (1)) to estimated rate constant parameters of tumor and muscle, respectively, in ETM. In RRM, only $C_{tumor}(t)$ and $C_{muslce}(t)$ were used to solve the relative rate constants. Based on the measured rate constant in muscle in ETM, absolute values of tumor parameters were calculated in RRM. Derived parameters with an R-squared value of < 0.8 in fitting ETM and RRM were excluded.

2.5. Pathology and immunohistochemistry

Tumor xenografts from treated animals were harvested and fixed into paraffin blocks. The paraffin embedded tissue slides were then processed and stained with either hematoxylin & eosin (H&E) or anti-CD31 (AbCam ab28364) for angiogenesis [46]. Formalin-fixed, paraffin-embedded tumors were cut into 4 μm sections and put onto slides. After the slides were deparaffinized and rehydrated, antigen retrieval was performed in a pressure cooker for 20 min in 0.5 M Tris buffer (pH 10). After H_2O_2 quench and 3 % horse serum blocking, slides were incubated with the primary antibody at 1:200 dilution for 20 min followed by anti-rabbit HRP (AbCam) for 20 min and Diaminobenzidine (DAB; Scy Tek Laboratories, Logan, UT) for 7 min. Slides were counterstained with hematoxylin. Hematoxylin and eosin safranin staining was performed on all the xenografts for morphology.

2.6. *Statistical analysis*

The Student’s T-test was used to compare the K^{trans} and K_{ep} values of tumor and muscle. Spearman’s correlation analysis was used to determine, r^2 and *P* values between K^{trans}, K_{ep} of the ETM and RRM, as well as their correlations to AUC, Hb, HbO_2, and SO_2. $P < 0.05$ was considered statistically significant.

3. Results

3.1. *Dynamic MSOT imaging of 2-DG-800 distribution in mice bearing breast cancer xenografts*

In our dynamic MSOT imaging, spectral unmixing, by referring to distinctive photothermal spectral behaviors of endogenous chromophores, such as Hb, and HbO_2 (which can be used to derive SO_2), as well as the 2-DG-800 probe (Fig. 1**A**), allowed us to monitor 2-DG-800 pharmacokinetics without being influenced by endogenous signals. We focused on spinal aorta and muscle in addition to tumor (with ROIs shown in Fig. 1**B**), as those areas were critical for deriving hemodynamic parameters of tumor using two-compartment models including ETM and RRM, respectively. To enable dynamic pharmacokinetic modeling of 2-DG-800 within tumors, we intravenously injected 10 nmol of 2-DG-800 after acquiring a 4-min baseline, with axial images of the mouse acquired during the imaging process at the location of the breast tumor. The scan lasted 40 min in total (Fig. 1**C**). Following injection of 2-DG-800 at 4 min, spikes of aorta signal became prominent at 5 min (Fig. 1**D&E**). Tumor and muscle also demonstrated initial increases after injection, followed a plateau, with markedly more probe accumulation in tumor than muscle (Fig. 1**D**). Tumor can also be readily identified in area-under-curve (AUC) (0–40 min) maps (Fig. 1**F**) because of significant contrast between tumor and normal tissues, such as muscle (Fig. 1**G**, $P = 0.039$, $n = 4$, paired Student’s t-test).

3.2. *Dynamic pharmacokinetic modeling of 2-DG-800 in tumor*

The extended Tofts model (ETM) (Fig. 2**A**) and non-linear reference region model (RRM) (Fig. 2**B**) were fitted to the empirical data points in a voxel-wise manner by optimizing the relevant rate constants. The K^{trans} values of voxels in tumor derived from the two models demonstrated a strong resemblance (Fig. 2**C**), so did K_{ep} values (Fig. 2**D**). Indeed, significant correlations can be found for voxel values of K^{trans} (Fig. 2**E**) and K_{ep} (Fig. 2**F)** between the two models, despite weaker correlations of K_{ep} values of the two models (correlation coefficient (r^2) = 0.736 for K^{trans} and $r^2 = 0.294$ for K_{ep}, data points were acquired from four mice).

We next assessed the value of K^{trans}(ETM) and K_{ep}(ETM) in detecting tumor. As shown in Fig. 3**A&B**, K^{trans}(ETM) values showed a positive linear correlation with AUC values ($r^2 = 0.552$). While K_{ep}(ETM) values were negatively correlated with AUC values, the correlation was quite weak ($r^2 = 0.129$). In the ROI-based analysis, both models indicated markedly higher K^{trans}(ETM) values ($P = 0.0398$, $n = 4$, paired t-test) and lower K_{ep}(ETM) values ($P = 0.0031$, $n = 4$, paired t-test) in tumors compared to muscles (Fig. 4**A&B**), suggesting that K^{trans} and K_{ep} derived from DGE-MSOT were both significant metrics for differentiating tumor and muscles.

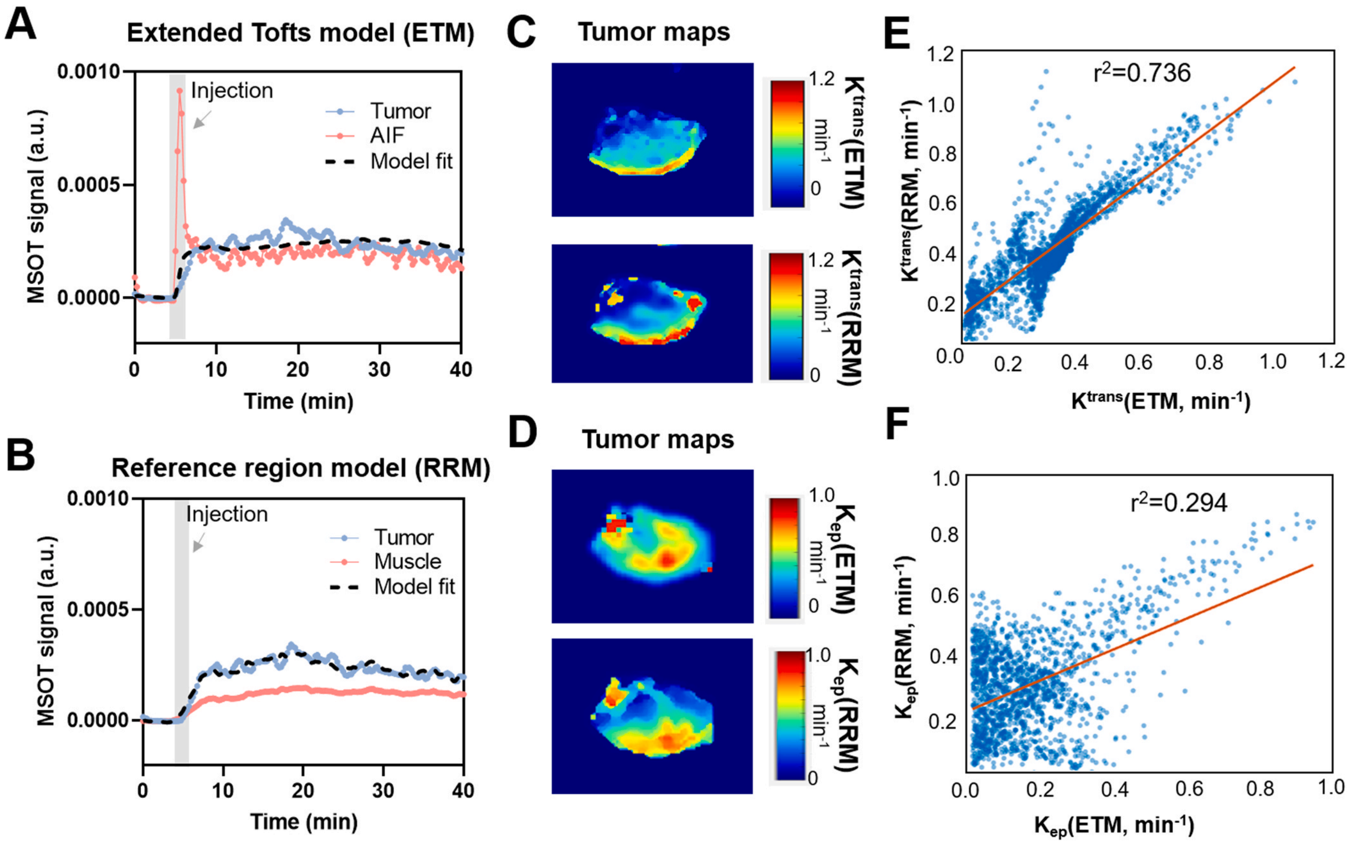

Fig. 2. Intratumoral pharmacokinetic modeling using the extended Tofts model (ETM) and reference region models (RRM). (**A,B**): Representative dynamic MSOT signal curves using ETM (**A**) and RRM (**B**). (**C,D**): tumor K^{trans} (**C**) and K_{ep} (**D**) maps using ETM and RRM. (**E,F**): Pearson’s correlation analyses showing strong positive linear correlations between K^{trans}(ETM) and K^{trans}(RRM) (**E**), and K_{ep}(ETM) and K_{ep}(RRM)(**F**). Scatter points in (**E**) and (**F**) were tumor voxel values acquired from four mice.

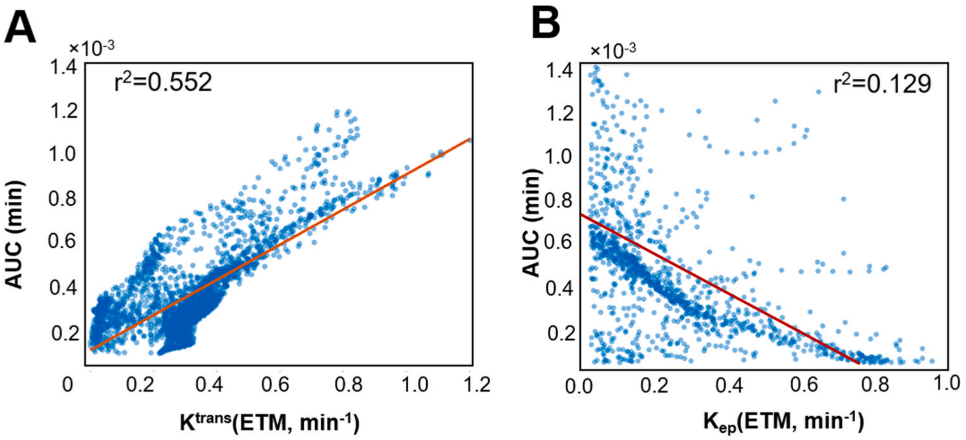

Fig. 3. Correlations of tumor K^{trans} and K_{ep} values from ETM model to AUC values. Scatter points were tumor voxel values acquired from four mice.

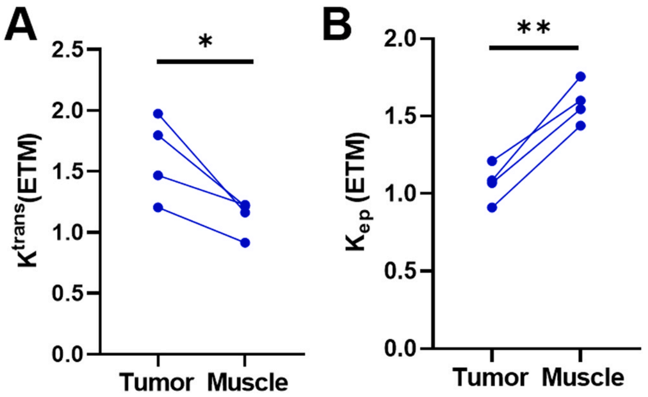

Fig. 4. Comparison of K^{trans} and K_{ep} values of tumor vs. muscle acquired from the extended Tofts model (ETM). *: $P = 0.0398$, **: $P = 0.0031$. n = 4, paired Student's t-test.

3.3. Correlations between pharmacokinetic parameters to oxygen-related endogenous chromophore levels

We next examined the correlations of K^{trans}(ETM), as a representative hemodynamic parameter, to levels of endogenous chromophores, including deoxyhemoglobin (Hb, Fig. 5**A,B**), oxyhemoglobin (HbO_2, **Fig. C,D**), and SO_2 (Fig. 5**E,F**). The Hb, HbO_2, and SO_2 maps of the tumor showed distinctive features of the tumor indicative of tumor oxygenation status. Overall, our data suggested that K^{trans} values were significantly but weakly correlated with Hb, HbO_2, and SO_2 values. Particularly, the weak correlations between SO_2 and K^{trans}(ETM) suggested that vasculature permeability and blood oxygen levels did not develop synchronically. These data suggest that DGE-MSOT is able to provide information about the tumor in addition to oxygenation parameters, which could be important to comprehensively unveil tumor characteristics associated with its aggressiveness.

4. Discussion

Here we explore the use of 2-DG-800 for dynamic pharmacokinetic modeling of breast tumors in MSOT. Our data suggest this new imaging tool is versatile in simultaneously evaluating glucose metabolism and tumor vasculature properties, which are two fundamental hallmarks of cancer characteristic of the tumor progression and responses to treatment capabilities. To date, only a few studies have explored simultaneous metabolism and vascularity assessment, predominantly by multimodal [^{18}F]FDG PET/MRI, which despite demonstrating a high prognostic value, involve separately injecting two contrast agents [47–49]. Compared to dynamic pharmacokinetic modeling methods in MRI and PET, which are relatively more established methods, pharmacokinetic modeling in MSOT is rarely explored because MSOT as an in vivo imaging modality is still in its infancy. The lack of ionizing radiation, and the ability to perform frequent tumor monitoring at the bedside, give MSOT advantages in facilitating timely clinical management of cancer [22]. The high sensitivity of MSOT also allows the use of a low dose probe (10 nmol per mouse, or 0.5 μmol/kg), which is much lower than the dose used for MRI, i.e., 0.1–1 mmol Gd/kg [50].

The suitability of MSOT in dynamic pharmacokinetic modeling also lies in its high temporal and spatial resolution. Our full-spectrum dynamic MSOT (680–900 nm with a step-size of 5 nm) has a temporal resolution of 15 s, acquiring axial slices of mice at the resolution of 75 μm × 75 μm × 0.1 mm, with 20 repetitions at each wavelength [51,52]. The high spatial resolution, which synergizes with the intrinsic high contrast of vasculatures in MSOT, allows us to accurately segment arteries to acquire AIF, as well as precisely quantify intratumoral hemodynamic parameters at a much finer scale. Although some DCE-MRI studies use a higher temporal resolution (~ 3–4 s) [53,54] than our study (temporal resolution of 15 s), single MSOT scan at each wavelength only took less than 7.5 ms, making MSOT scans less susceptible to motion artifacts, and further optimization to reduce the number of wavelengths and repetitions has potential to dramatically decrease temporal resolution without compromising spatial resolution.

To improve upon our previous method in intratumoral pharmacokinetic modeling of an optoacoustic probe, HS680, the present study systemically studied tumor pharmacokinetic parameters using 2-DG-800 in a voxel-wise manner. Compared to the previous ROI-based analysis, the approach established in the current study enabled voxel-by-voxel comparison of two popular pharmacokinetic models, ETM [39] and RRM, but also made it possible to evaluate the correlation of these parameters to the oxygenation status of the tumor.

RRM has been developed as an alternative to Tofts models to eliminate the need for acquiring AIF as tumor and arteries may not be present in the same field of view, making accurately measuring AIF challenging [55]. RR model replaces AIF with a differential equation depicting the time-dependent contrast concentration in a well-characterized reference region, typically muscles. Because MSOT excels at detecting arterial signals and the axial images in our scans covered easily identifiable spinal aorta, ETM was used as a gold standard in our study. Despite this, for scanning areas where the arterial signal is not present, RRM could be advantageous, and comparing the robustness of RRM is critical. In our study, K^{trans} and K_{ep} values derived from both models were significantly correlated, although the correlation of K_{ep} values derived from the two models was relatively weaker. By comparing parametric maps of the ETM and RRM, we found that RRM presented less homogenous intratumoral parameters (see Fig. 2). This could arise from the lower muscle

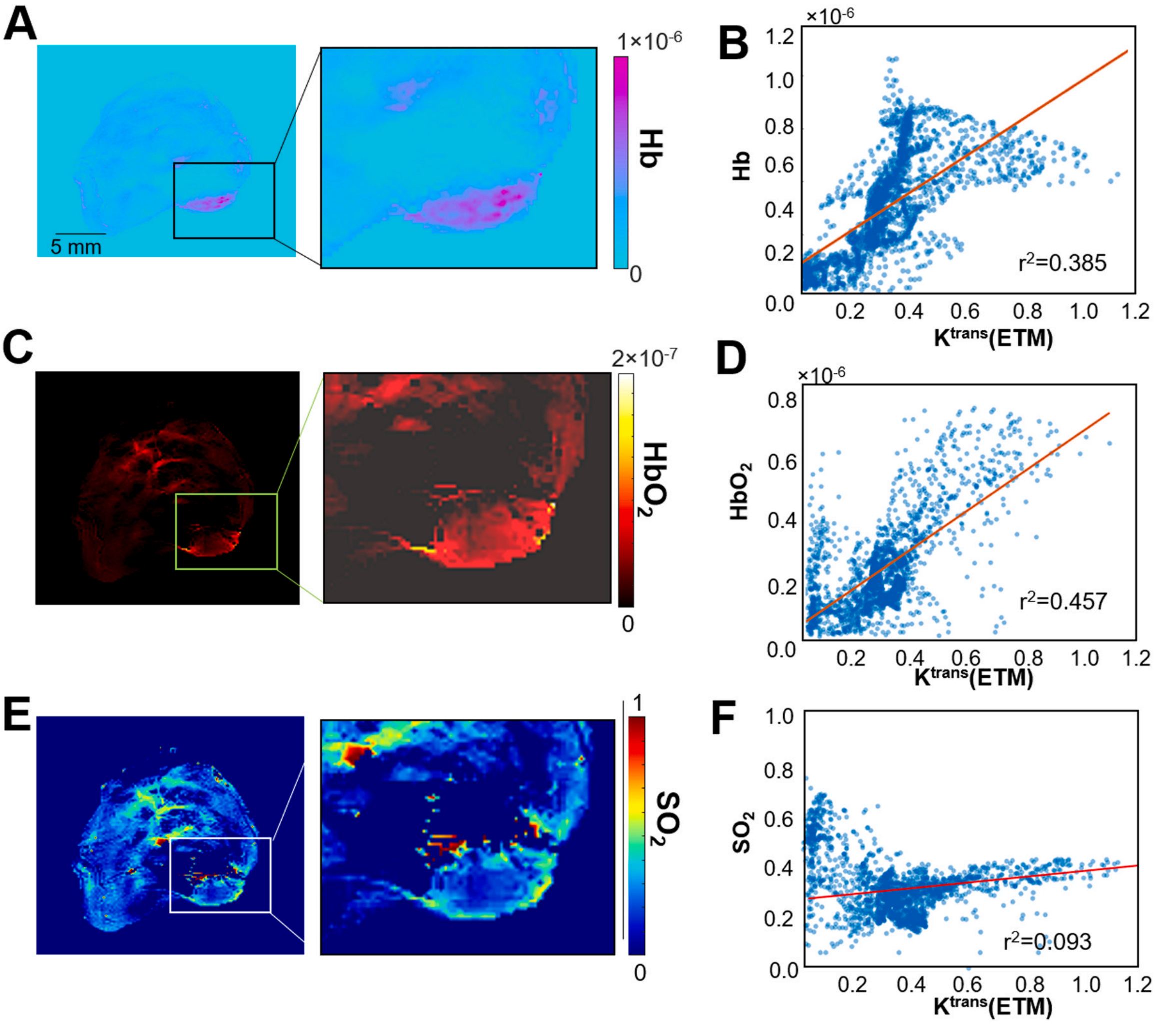

Fig. 5. Correlations between pharmacokinetic parameters to endogenous chromophore levels. (A,C,E) Representative unmixed deoxy-hemoglobin (Hb) (**A**), oxyhemoglobin (HbO_2) (**C**), and SO_2 (**E**) maps. (**B,D,F**) Correlational analyses of K^{trans} values to Hb (**B**), HbO_2 (**D**), and SO_2 (**F**). Scatter points were tumor voxel values acquired from four mice after excluding non-positive voxels in all parameter maps.

signal, which led to lower signal-to-noise (SNR) of muscle signals than the arterial signals. Notably, the correlation coefficients of K^{trans} values from the two models were higher than that of the K^{ep} values, which has also been observed in previous studies [56]. One distinctive difference between DGE-MSOT and DCE-MRI is that 2-DG-800 is actively transported across the cellular membrane, whereas gadolinium-based contrast agents remain in the blood pool [57,58]. Therefore, the K^{trans} of DGE-MSOT is reflective of mixed influx of agents into tumor and intracellular transportation, which, in cells with high metabolic activity, leads to an overestimation of the K^{trans}.

The voxel-based analysis also allowed us to study intratumoral metabolic, hemodynamic, and oxygenation heterogeneity, which are potentially strong predictors of patient survival [59,60]. The high intratumoral heterogeneity observed in our study agrees with the highly aggressive nature of the 2-LMP triple-negative breast cancer cell line. This heterogeneity was confirmed using tissue morphology and angiogenesis was confirmed with CD31 (Fig. 6). In addition, the voxel-based approach allowed us to examine correlations between parameters to comprehensively characterize the tumor. AUC and K^{trans} acquired in our study were strongly correlated (see Fig. 3), suggesting that tumor cells with high metabolism develop permeabilized vessels and that provide sufficient nutrient supply to keep up with metabolism. Meanwhile, correlations of K^{trans} to tumor oxygenation (i.e., high HbO_2, and SO_2 levels) were relatively weak (despite being significant), indicating that in different parts of the tumor, oxygen may or may not keep up with neovascularization, a piece of evidence that tumors could have varying levels of hypoxia.

It is worth noting that the emerging dynamically enhanced MSOT technique can be extended to applications that other dynamically enhanced imaging technologies have explored. For example, O'Connor et al. have combined DCE and oxygen-enhanced (OE)-MRI to explore tumor hypoxia, and OE-MRI was shown to be capable of quantifying the hypoxic fraction in multiple models with differing hypoxic and vascular phenotypes. OE-MRI was also shown to detect dynamic changes in hypoxia induced by the vasomodulator agent [61]. Further, given the link between hypoxia and tumor response to radiation therapy, oxygen-sensitive MRI could also assist in response monitoring and outcome prediction during radiation therapy [62]. Similarly, oxygen-enhanced MSOT (OE-MSOT) and other hypoxia-sensitive MSOT techniques [37,63,64] demonstrated comparable capabilities to monitor tumor oxygenation in real-time, and the unique strengths of MSOT, including portability, high spatiotemporal resolution, etc., potentiates its application in certain clinical settings infeasible for MRI and other imaging modalities. It should, however, be noted that the labeling of 2-DG with IRDye800 alters the metabolism of 2-DG and may not dynamically reflect glucose metabolism, in contrast to MRI technologies that require no labeling for dynamic imaging, e.g., chemical exchange saturation transfer (CEST) MRI [65]. Moreover, in this pharmacokinetic

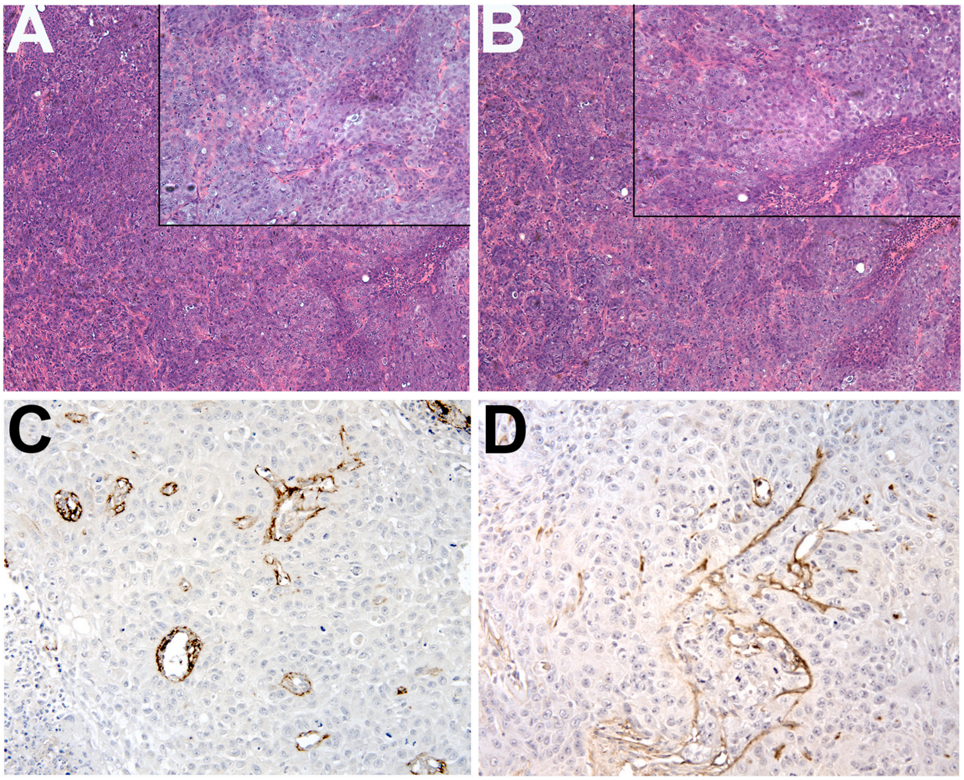

Fig. 6. Pathology and immunohistochemistry. Tumors were assessed for morphology as well as angiogenesis using H&E staining as well as immunohistochemistry. **(A–B)** Hematoxylin and Eosin staining of breast tumor xenografts. Images taken with a 4 × objective and inserts taken at 20 × **(C–D)** Angiogenesis assessed using anti-CD31 in breast tumor xenografts. Images taken with 40 × objective. Brown staining indicates CD31 positive areas (angiogenesis).

study, we did not measure the clearance of the probe, and further studies that monitor probe clearance in a longer time frame are needed for clinical translation.

In summary, here we explored a novel method for dynamic modeling of 2-DG-800 pharmacokinetics in tumor using MSOT. The use of 2-DG-800 enabled the simultaneous measurement of tumor glucose transporter activity, as a surrogate marker for glucose metabolism, in addition to hemodynamics, and the voxel-wise analyses of parameters derived from both ETM and RRM suggested the utility of both models for analyzing DGE-MSOT data. As many dye-labeled anti-cancer drugs have been studied in clinical trials (NCT02415881, NCT02855086), our approach can also be expanded to understanding the drugs' intratumoral kinetics.

Declaration of Competing Interest

The authors declare that they have no known competing financial interests or personal relationships that could have appeared to influence the work reported in this paper.

Data Availability

Data will be made available on request.

Acknowledgment

Research reported in this publication was supported in part by R01CA205941, R01EB034731, R01CA241156, and a Stephenson Cancer Center Trainee Research Award funded by the National Cancer Institute Cancer Center Support Grant P30CA225520. The content is solely the responsibility of the authors and does not necessarily represent the official views of the National Institutes of Health.

Appendix A. Supporting information

Supplementary data associated with this article can be found in the online version at doi:10.1016/j.pacs.2023.100531.

References

[1] F. Kreis, A.J. Wright, F. Hesse, M. Fala, D.E. Hu, K.M. Brindle, Measuring tumor glycolytic flux in vivo by using fast deuterium MRI, Radiology 294 (2) (2020) 289–296.

[2] D. Paech, P. Schuenke, C. Koehler, J. Windschuh, S. Mundiyanapurath, S. Bickelhaupt, D. Bonekamp, P. Baumer, P. Bachert, M.E. Ladd, M. Bendszus, W. Wick, A. Unterberg, H.P. Schlemmer, M. Zaiss, A. Radbruch, T1rho-weighted dynamic glucose-enhanced MR imaging in the human brain, Radiology 285 (3) (2017) 914–922.

[3] C. Bouron, C. Mathie, V. Seegers, O. Morel, P. Jezequel, H. Lasla, C. Guillerminet, S. Girault, M. Lacombe, A. Sher, F. Lacoeuille, A. Patsouris, A. Testard, Prognostic value of metabolic, volumetric and textural parameters of baseline [(18)F]FDG PET/CT in early triple-negative breast cancer, Cancers 14 (3) (2022).

[4] M.K. Ravoori, S.P. Singh, J. Lee, J.A. Bankson, V. Kundra, In vivo assessment of ovarian tumor response to tyrosine kinase inhibitor pazopanib by using hyperpolarized C-13-pyruvate MR spectroscopy and F-18-FDG PET/CT imaging in a mouse model, Radiology 285 (3) (2017) 830–838.

[5] G. Komar, S. Kauhanen, K. Liukko, M. Seppanen, S. Kajander, J. Ovaska, P. Nuutila, H. Minn, Decreased blood flow with increased metabolic activity: a novel sign of pancreatic tumor aggressiveness, Clin. Cancer Res. 15 (17) (2009) 5511–5517.

[6] C.W. Michalski, M. Erkan, H. Friess, J. Kleeff, Tumor metabolism to blood flow ratio in pancreatic cancer: helpful in patient stratification? Future Oncol. 6 (1) (2010) 13–15.

[7] M.C. Skala, A. Fontanella, L. Lan, J.A. Izatt, M.W. Dewhirst, Longitudinal optical imaging of tumor metabolism and hemodynamics, J. Biomed. Opt. 15 (1) (2010), 011112.

[8] L.J. Rich, M. Seshadri, Photoacoustic imaging of vascular hemodynamics: validation with blood oxygenation level-dependent MR imaging, Radiology 275 (1) (2015) 110–118.

[9] J.H. Zhang, Y.Y. Chen, Y.Y. Zhang, E.L. Zhang, H.J. Yu, H.S. Yuan, Y. Zhang, M. Y. Su, N. Lang, Diagnosis of spinal lesions using perfusion parameters measured by DCE-MRI and metabolism parameters measured by PET/CT, Eur. Spine J. 29 (5) (2020) 1061–1070.

[10] M. Inglese, C. Cavaliere, S. Monti, E. Forte, M. Incoronato, E. Nicolai, M. Salvatore, M. Aiello, A multi-parametric PET/MRI study of breast cancer: evaluation of DCE-

MRI pharmacokinetic models and correlation with diffusion and functional parameters, Nmr Biomed. 32 (1) (2019).

[11] G.A. Kaissis, F.K. Lohofer, M. Horl, I. Heid, K. Steiger, K.A. Munoz-Alvarez, M. Schwaiger, E.J. Rummeny, W. Weichert, P. Paprottka, R. Braren, Combined DCE-MRI- and FDG-PET enable histopathological grading prediction in a rat model of hepatocellular carcinoma, Eur. J. Radiol. 124 (2020).

[12] N. Jahani, E. Cohen, M.K. Hsieh, S.P. Weinstein, L. Pantalone, N. Hylton, D. Newitt, C. Davatzikos, D. Kontos, Prediction of treatment response to neoadjuvant chemotherapy for breast cancer via early changes in tumor heterogeneity captured by DCE-MRI registration, Sci. Rep. 9 (2019).

[13] N.M. Braman, M. Etesami, P. Prasanna, C. Dubchuk, H. Gilmore, P. Tiwari, D. Plecha, A. Madabhushi, Intratumoral and peritumoral radiomics for the pretreatment prediction of pathological complete response to neoadjuvant chemotherapy based on breast DCE-MRI, Breast Cancer Res. 19 (1) (2017) 57.

[14] Y. Yang, J. Li, Y. Liu, Y. Zhong, W. Ren, Y. Tan, Z. He, C. Li, J. Ouyang, Q. Hu, Y. Yu, H. Yao, Magnetic resonance imaging radiomics signatures for predicting endocrine resistance in hormone receptor-positive non-metastatic breast cancer, Breast 60 (2021) 90–97.

[15] M. Ramalho, J. Ramalho, L.M. Burke, R.C. Semelka, Gadolinium retention and toxicity–an update, Adv. Chronic Kidney Dis. 24 (3) (2017) 138–146.

[16] L. Pasquini, A. Napolitano, E. Visconti, D. Longo, A. Romano, P. Toma, M.C. Rossi, Espagnet, gadolinium-based contrast agent-related toxicities, CNS Drugs 32 (3) (2018) 229–240.

[17] J. Ramalho, M. Ramalho, Gadolinium deposition and chronic toxicity, Magn. Reson Imaging Clin. N. Am. 25 (4) (2017) 765–778.

[18] F.L. Besson, B. Fernandez, S. Faure, O. Mercier, A. Seferian, X. Mignard, S. Mussot, C. le Pechoux, C. Caramella, A. Botticella, 18F-FDG PET and DCE kinetic modeling and their correlations in primary NSCLC: first voxel-wise correlative analysis of human simultaneous [18F] FDG PET-MRI data, Ejnmmi Res. 10 (1) (2020) 1–13.

[19] H. Zhou, K. Luby-Phelps, B.E. Mickey, A.A. Habib, R.P. Mason, D. Zhao, Dynamic near-infrared optical imaging of 2-deoxyglucose uptake by intracranial glioma of athymic mice, PLoS One 4 (11) (2009), e8051.

[20] L.R. McNally, M. Mezera, D.E. Morgan, P.J. Frederick, E.S. Yang, I.E. Eltoum, W. E. Grizzle, Current and emerging clinical applications of multispectral optoacoustic tomography (MSOT) in oncology, clinical cancer research: an official journal of the American Association for, Cancer Res. 22 (14) (2016) 3432–3439.

[21] I.S. Dennahy, Z. Han, W.M. MacCuaig, H.M. Chalfant, A. Condacse, J.M. Hagood, J. C. Claros-Sorto, W. Razaq, J. Holter-Chakrabarty, R. Squires, B.H. Edil, A. Jain, L. R. McNally, Nanotheranostics for image-guided cancer treatment, Pharmaceutics 14 (5) (2022).

[22] W.M. MacCuaig, M.A. Jones, O. Abeyakoon, L.R. McNally, Development of multispectral optoacoustic tomography as a clinically translatable modality for cancer imaging, Radiol.: Imaging Cancer 2 (6) (2020), e200066.

[23] I. Stoffels, S. Morscher, I. Helfrich, U. Hillen, J. Lehy, N.C. Burton, T.C. Sardella, J. Claussen, T.D. Poeppel, H.S. Bachmann, Metastatic status of sentinel lymph nodes in melanoma determined noninvasively with multispectral optoacoustic imaging, Sci. Transl. Med. 7 (317) (2015), 317ra199-317ra199.

[24] F. Knieling, C. Neufert, A. Hartmann, J. Claussen, A. Urich, C. Egger, M. Vetter, S. Fischer, L. Pfeifer, A. Hagel, C. Kielisch, R.S. Gortz, D. Wildner, M. Engel, J. Rother, W. Uter, J. Siebler, R. Atreya, W. Rascher, D. Strobel, M.F. Neurath, M. J. Waldner, Multispectral optoacoustic tomography for assessment of Crohn's disease activity, N. Engl. J. Med. 376 (13) (2017) 1292–1294.

[25] S.V. Hudson, J.S. Huang, W.Y. Yin, S. Albeituni, J. Rush, A. Khanal, J. Yan, B. P. Ceresa, H.B. Frieboes, L.R. McNally, Targeted noninvasive imaging of EGFR-expressing orthotopic pancreatic cancer using multispectral optoacoustic tomography, Cancer Res. 74 (21) (2014) 6271–6279.

[26] D. Razansky, J. Baeten, V. Ntziachristos, Sensitivity of molecular target detection by multispectral optoacoustic tomography (MSOT), Med. Phys. 36 (3) (2009) 939–945.

[27] M.J. Waldner, F. Knieling, C. Egger, S. Morscher, J. Claussen, M. Vetter, C. Kielisch, S. Fischer, L. Pfeifer, A. Hagel, R.S. Goertz, D. Wildner, R. Atreya, D. Strobel, M. F. Neurath, Multispectral optoacoustic tomography in Crohn's disease: noninvasive imaging of disease activity, Gastroenterology 151 (2) (2016) 238–240.

[28] S. Dey, S. Kumari, S.P. Kalainayakan, J. Campbell III, P. Ghosh, H. Zhou, K. E. FitzGerald, M. Li, R.P. Mason, L. Zhang, The vascular disrupting agent combretastatin A-4 phosphate causes prolonged elevation of proteins involved in heme flux and function in resistant tumor cells, Oncotarget 9 (3) (2018) 4090.

[29] C.W. Hupple, S. Morscher, N.C. Burton, M.D. Pagel, L.R. McNally, J. Cardenas-Rodriguez, A light-fluence-independent method for the quantitative analysis of dynamic contrast-enhanced multispectral optoacoustic tomography (DCE MSOT), Photoacoustics 10 (2018) 54–64.

[30] A.P. Regensburger, L.M. Fonteyne, J. Jüngert, A.L. Wagner, T. Gerhalter, A. M. Nagel, R. Heiss, F. Flenkenthaler, M. Qurashi, M.F. Neurath, N. Klymiuk, E. Kemter, T. Fröhlich, M. Uder, J. Woelfle, W. Rascher, R. Trollmann, E. Wolf, M. J. Waldner, F. Knieling, Detection of collagens by multispectral optoacoustic tomography as an imaging biomarker for Duchenne muscular dystrophy, Nat. Med. 25 (12) (2019) 1905–1915.

[31] M.D. Laramie, B.L. Fouts, W.M. MacCuaig, E. Buabeng, M.A. Jones, P. Mukherjee, B. Behkam, L.R. McNally, M. Henary, Improved pentamethine cyanine nanosensors for optoacoustic imaging of pancreatic cancer, Sci. Rep. 11 (1) (2021) 4366.

[32] W.M. MacCuaig, B.L. Fouts, M.W. McNally, W.E. Grizzle, P. Chuong, A. Samykutty, P. Mukherjee, M. Li, J.B. Jasinski, B. Behkam, L.R. McNally, Active targeting significantly outperforms nanoparticle size in facilitating tumor-specific uptake in orthotopic pancreatic cancer, ACS Appl. Mater. Interfaces 13 (42) (2021) 49614–49630.

[33] M.D. Laramie, M.K. Smith, F. Marmarchi, L.R. McNally, M. Henary, Small molecule optoacoustic contrast agents: an unexplored avenue for enhancing in vivo imaging, Molecules 23 (11) (2018).

[34] W. Yin, C.W. Kimbrough, J.G. Gomez-Gutierrez, C.T. Burns, P. Chuong, W. E. Grizzle, L.R. McNally, Tumor specific liposomes improve detection of pancreatic adenocarcinoma in vivo using optoacoustic tomography, J. Nanobiotechnol. 13 (1) (2015) 90.

[35] A. Thomas, A. Samykutty, J.G. Gomez-Gutierrez, W. Yin, M.E. Egger, M. McNally, P. Chuong, W.M. MacCuaig, S. Albeituni, M. Zeiderman, M. Li, B.H. Edil, W. E. Grizzle, K.M. McMasters, L.R. McNally, Actively targeted nano-delivery of echinomycin induces autophagy mediated death in chemoresistant pancreatic cancer in vivo, Cancers 12 (8) (2020) 2279.

[36] A. Khanal, C. Ullum, C. Kimbrough, N. Garbett, J. Burlison, M. McNally, P. Chuong, A. El-Baz, J. Jasinski, L. McNally, Tumor targeted mesoporous silica-coated gold nanorods facilitate detection of pancreatic tumors using multispectral optoacoustic tomography, Nano Res. 8 (12) (2015) 3864–3877.

[37] T.G. Xiao, J.A. Weis, F.S. Gayzik, A. Thomas, A. Chiba, M.N. Gurcan, U. Topaloglu, A. Samykutty, L.R. McNally, Applying dynamic contrast enhanced MSOT imaging to intratumoral pharmacokinetic modeling, Photoacoustics 11 (2018) 28–35.

[38] A.B. Attia, C.J. Ho, P. Chandrasekharan, G. Balasundaram, H.C. Tay, N.C. Burton, K.H. Chuang, V. Ntziachristos, M. Olivo, Multispectral optoacoustic and MRI coregistration for molecular imaging of orthotopic model of human glioblastoma, J. Biophotonics 9 (7) (2016) 701–708.

[39] S.P. Sourbron, D.L. Buckley, On the scope and interpretation of the Tofts models for DCE-MRI, Magn. Reson. Med. 66 (3) (2011) 735–745.

[40] J. Cardenas-Rodriguez, C.M. Howison, M.D. Pagel, A linear algorithm of the reference region model for DCE-MRI is robust and relaxes requirements for temporal resolution, Magn. Reson. Imaging 31 (4) (2013) 497–507.

[41] H. Liu, K. Wang, D. Peng, H. Li, Y. Zhu, S. Zhang, M. Liu, J. Tian, Curve-driven-based acoustic inversion for photoacoustic tomography, IEEE Trans. Med. Imaging 35 (12) (2016) 2546–2557.

[42] D. O'Kelly, J. Campbell, 3rd, J.L. Gerberich, P. Karbasi, V. Malladi, A. Jamieson, L. Wang, R.P. Mason, A scalable open-source MATLAB toolbox for reconstruction and analysis of multispectral optoacoustic tomography data, Sci. Rep. 11 (1) (2021) 19872.

[43] A.L. Bendinger, C. Glowa, J. Peter, C.P. Karger, Photoacoustic imaging to assess pixel-based sO2 distributions in experimental prostate tumors, J. Biomed. Opt. 23 (3) (2018) 1–11.

[44] J. Cárdenas-Rodríguez, C.M. Howison, M.D. Pagel, A linear algorithm of the reference region model for DCE-MRI is robust and relaxes requirements for temporal resolution, Magn. Reson Imaging 31 (4) (2013) 497–507.

[45] J. Xia, J. Yao, L.V. Wang, Photoacoustic tomography: principles and advances, Electromagn. Waves 147 (2014) 1–22.

[46] J.J. Lee, J. Huang, C.G. England, L.R. McNally, H.B. Frieboes, Predictive modeling of in vivo response to gemcitabine in pancreatic cancer, PLoS Comput. Biol. 9 (9) (2013), e1003231.

[47] A. Jena, S. Taneja, A. Singh, P. Negi, S.B. Mehta, R. Sarin, Role of pharmacokinetic parameters derived with high temporal resolution DCE MRI using simultaneous PET/MRI system in breast cancer: a feasibility study, Eur. J. Radiol. 86 (2017) 261–266.

[48] S.J. Hectors, M. Wagner, C. Besa, W. Huang, B. Taouli, Multiparametric FDG-PET/MRI of hepatocellular carcinoma: initial experience, Contrast Media Mol. Imaging 2018 (2018) 5638283.

[49] J.H. Rasmussen, A. Olin, G. Lelkaitis, A.E. Hansen, F.L. Andersen, H. H. Johannesen, A. Kjaer, I.R. Vogelius, L. Specht, S.M. Bentzen, I. Wessel, C. von Buchwald, B.M. Fischer, Does multiparametric imaging with (18)F-FDG-PET/MRI capture spatial variation in immunohistochemical cancer biomarkers in head and neck squamous cell carcinoma? Br. J. Cancer 123 (1) (2020) 46–53.

[50] J.A. Jakobsen, C.C. Quattrocchi, F.H.H. Muller, O. Outteryck, A. Alcazar, W. Reith, P. Fraga, V. Panebianco, A. Sampedro, R. Pietura, Patterns of use, effectiveness and safety of gadolinium contrast agents: a European prospective cross-sectional multicentre observational study, Bmc Med. Imaging 21 (1) (2021).

[51] N. Bhutiani, C.W. Kimbrough, N.C. Burton, S. Morscher, M. Egger, K. McMasters, A. Woloszynska-Read, A. El-Baz, L.R. McNally, Detection of microspheres in vivo using multispectral optoacoustic tomography, Biotech. Histochem.: Off. Publ. Biol. Stain Comm. 92 (1) (2017) 1–6.

[52] A. Samykutty, K.N. Thomas, M. McNally, J. Hagood, A. Chiba, A. Thomas, L. McWilliams, B. Behkam, Y. Zhan, M. Council-Troche, J.C. Claros-Sorto, C. Henson, T. Garwe, Z. Sarwar, W.E. Grizzle, L.R. McNally, Simultaneous detection of multiple tumor-targeted gold nanoparticles in HER2-positive breast tumors using optoacoustic imaging, Radiol. Imaging Cancer 5 (3) (2023), e220180.

[53] L. Georgiou, D.J. Wilson, N. Sharma, T.J. Perren, D.L. Buckley, A functional form for a representative individual arterial input function measured from a population using high temporal resolution DCE MRI, Magn. Reson. Med. 81 (3) (2019) 1955–1963.

[54] M. Kataoka, M. Honda, A. Ohashi, K. Yamaguchi, N. Mori, M. Goto, T. Fujioka, M. Mori, Y. Kato, H. Satake, Ultrafast dynamic contrast-enhanced MRI of the breast: how is it used? Magn. Reson. Med. Sci. 21 (1) (2022) 83–94.

[55] T.E. Yankeelov, G.O. Cron, C.L. Addison, J.C. Wallace, R.C. Wilkins, B.A. Pappas, G.E. Santyr, J.C. Gore, Comparison of a reference region model with direct measurement of an AIF in the analysis of DCE-MRI data, Magn. Reson. Med. 57 (2) (2007) 353–361.

[56] Z. Ahmed, I.R. Levesque, An extended reference region model for DCE-MRI that accounts for plasma volume, Nmr Biomed. 31 (7) (2018).

[57] B. Pajak, E. Siwiak, M. Soltyka, A. Priebe, R. Zielinski, I. Fokt, M. Ziemniak, A. Jaskiewicz, R. Borowski, T. Domoradzki, W. Priebe, 2-Deoxy-D-glucose and its analogs: from diagnostic to therapeutic agents, Int. J. Mol. Sci. 21 (1) (2019).

[58] A.M. Mohs, Z.R. Lu, Gadolinium(III)-based blood-pool contrast agents for magnetic resonance imaging: status and clinical potential, Expert Opin. Drug Deliv. 4 (2) (2007) 149–164.

[59] A. Marra, D. Trapani, G. Viale, C. Criscitiello, G. Curigliano, Practical classification of triple-negative breast cancer: intratumoral heterogeneity, mechanisms of drug resistance, and novel therapies, NPJ Breast Cancer 6 (2020) 54.

[60] B.Z. Clark, A. Onisko, B. Assylbekova, X. Li, R. Bhargava, D.J. Dabbs, Breast cancer global tumor biomarkers: a quality assurance study of intratumoral heterogeneity, Mod. Pathol. 32 (3) (2019) 354–366.

[61] P. Ghosh, Y. Guo, A. Ashrafi, J. Chen, S. Dey, S. Zhong, J. Liu, J. Campbell, P. C. Konduri, J. Gerberich, Oxygen-enhanced optoacoustic tomography reveals the effectiveness of targeting heme and oxidative phosphorylation at normalizing tumor vascular oxygenation, Cancer Res. 80 (17) (2020) 3542–3555 (Normalizing tumor vascular function via heme targeting).

[62] T.J. Arai, D.M. Yang, J.W. Campbell, 3rd, T. Chiu, X. Cheng, S. Stojadinovic, P. Peschke, R.P. Mason, Oxygen-sensitive MRI: a predictive imaging biomarker for tumor radiation response? Int. J. Radiat. Oncol. Biol. Phys. 110 (5) (2021) 1519–1529.

[63] J. Huang, Y. Wu, F. Zeng, S. Wu, An activatable near-infrared chromophore for multispectral optoacoustic imaging of tumor hypoxia and for tumor inhibition, Theranostics 9 (24) (2019) 7313–7324.

[64] K.M. Harold, W.M. MacCuaig, J. Holter-Charkabarty, K. Williams, K. Hill, A. X. Arreola, M. Sekhri, S. Carter, J. Gomez-Gutierrez, G. Salem, G. Mishra, L. R. McNally, Advances in imaging of inflammation, fibrosis, and cancer in the gastrointestinal tract, Int. J. Mol. Sci. 23 (24) (2022) 16109.

[65] M. Rivlin, J. Horev, I. Tsarfaty, G. Navon, Molecular imaging of tumors and metastases using chemical exchange saturation transfer (CEST) MRI, Sci. Rep. 3 (1) (2013) 3045.

I am a Research Instructor in biomedical imaging and drug delivery systems, specializing in developing image-guided systems for precision diagnosis and treatment of cancer and other diseases. I have inter-disciplinarily skills in chemistry, biomedical imaging, and nanomedicine. I completed my Ph.D. at Case Western Reserve University and my post doc training at Johns Hopkins University. I focused on developing gadolinium-based and bioorganic Chemical Exchange Saturation Transfer (CEST) MRI probes with the potential of non-invasively delineating enzyme activity and tumor stroma formation, which are closely correlated with cancer aggressiveness. My current work at the University of Oklahoma Health Science Center involves development of contrast agents for optoacoustic imaging as well as image analysis. My other research interests also include developing smart nano-particle drug/gene delivery systems using mesoporous silica and lipids.